Theoretical Investigation of V_3C_2 MXene as Prospective High Capacity Anode Material for Metal (Li, Na, K, Ca) Ion Batteries

Ke Fan [a], *Yiran Ying* [a], *Xiaoyan Li* [a], *Xin Luo** [a,b], *and Haitao Huang** [a]

[a]Department of Applied Physics, The Hong Kong Polytechnic University, Hung Hom, Kowloon, Hong Kong, P.R. China

[b]School of Physics, Sun Yat-sen University, Guangzhou, Guangdong Province, P.R. China, 510275

AUTHOR INFORMATION

Corresponding Author

*E-mail: aphhuang@polyu.edu.hk (H.H.); luox77@mail.sysu.edu.cn (X.L.)

ABSTRACT. Two-dimensional (2D) transition metal carbides (MXenes) as electrode materials have attracted much attention due to their excellent energy storage properties and electrical conductivity. In this work, we study the properties of the V_3C_2 MXene anode for metal ion (Li, Na, K and Ca) batteries by means of density functional theory (DFT) computations. Based on our calculated results, V_3C_2 exhibits excellent properties such as structural stability, good electrical conductivity, fast charge-discharge rates, and high theoretical storage capacity. In particular, owing to its low diffusion barrier (0.04 eV for Li, 0.02 eV for Na, 0.01 eV for K, and 0.04 eV for Ca) and high storage capacity (606.42 mAh g^{-1} for both Li and Na, 269.86 mAh g^{-1} for K and 539.71 mAh g^{-1} for Ca), V_3C_2 monolayer is predicted to be a promising anode material especially for lithium-ion batteries (LIBs) and sodium-ion batteries (SIBs). Our work provides a new avenue for the design of novel 2D materials for energy applications.

MAIN TEXT

1. Introduction

Energy storage technology has been powering the world, with applications ranging from portable electronics to large-scale power grid systems.[1-3] Among various types of energy storage systems, lithium-ion batteries (LIBs), one of the greatest successes of clean energy storage technologies, have attracted widespread attention because of their excellent reversible capacity, high energy density, and long operational lifetime. However, due to the relatively low capacity and poor rate capability, their applications are still far from satisfactory.[4-8] The lack of lithium resources can be another obstacle which greatly hampers their development. Thus, lots of efforts have been devoted to developing new energy materials to meet the demand for the next generation metal-ion batteries, such as enhancing the efficiency of the LIBs or proposing new protocols. Since sodium is more earth-abundant and much cheaper than lithium, sodium-ion batteries (SIBs) are expected to be potential alternatives to LIBs in the future.[9-12] In addition, other alkali ions such as potassium and calcium, are also promising choices.[2, 13] Nevertheless, unconventional metal ion batteries with high capacity and rate capability are of immediate interest in the real world applications.

Electrode materials play a critical role in the performance of metal ion batteries.[2] Compared with the rapid development in cathode materials, the improvement of anode materials is much slower.[14] Nowadays, the most widely-used LIBs anode material is graphite, which is plagued by a relatively low capacity of 372 mAh g^{-1} and poor rate capability. Hence, its applications are greatly limited.[2, 10, 15-16] Fortunately, with the development of materials science, 2D materials with large surface-area-to-volume ratio are believed to be promising candidates for the anode materials in metal ion batteries.[3, 17-18] Until now, a few 2D materials, including transition metal dichalcogenides and

metal oxides, have been identified as potential anode materials with enhanced electronic properties for metal ion batteries.[4, 7, 19-23] Among these 2D electrode materials, the maximum capacity values for LIBs are beyond 350 mAh g^{-1}, comparable with the commercialized graphite electrodes. Nevertheless, exploring other novel 2D materials with higher storage capacities is still a burgeoning research area.[24]

More recently, a group of new 2D transition metal carbides, nitrides, or carbonitrides, called MXenes, have been reported and investigated as a new family of 2D materials.[25-29] MXenes can be produced by selectively etching the A layer from MAX phases (M, A, and X represent early transition metal, group IIIA/IVA element, and C/N, respectively) with hydrofluoric acid (HF) at room temperature.[30] The general chemical formula of the MAX phase is $M_{n+1}AX_n$ (n = 1, 2, or 3), forming MXenes with three different structures (M_2X, M_3X_2, or M_4X_3). Up to now, many kinds of MXenes have been predicted to show good performance as electrodes. Using DFT calculations, Er et al. found that the diffusion barrier of Li atoms on Ti_3C_2 (0.07 eV) is smaller than that for graphite.[2] Most recently, V_2C has been predicted to have a very high specific Li capacity and a low surface diffusion barrier.[31] The properties and applications of V_3C_2 MXene, on the other hand, have not been fully explored although it is predicted to be an ideal nitrogen reduction reaction catalyst[32]. The calculated V_3C_2 MXene exhibits high electrical conductivity, which might facilitate its potential application in metal ion batteries as its compositional analogue V_2C.

Inspired by the content discussed above, in this paper, we systematically investigate the stability, electronic and metal (Li/Na/K/Ca) storage properties of V_3C_2 monolayer by means of density functional theory (DFT) calculations. We also compare the results with the oxygen-functionalized V_3C_2. Our calculations reveal that V_3C_2 exhibits high storage capacity and low diffusion barriers,

suggesting that the V_3C_2 monolayer could be a promising anode material for metal ion batteries, especially for LIBs/SIBs.

2. Computational methods

First-principles density functional theory (DFT) calculations were performed by the Vienna *ab initio* simulation package (VASP)[33]. To optimize the geometric structures, the generalized gradient approximation (GGA) with the Perdew-Burke-Ernzerhof (PBE) flavor[34] was chosen as the exchange-correlation functional. The DFT plus long-range dispersion correction DFT-D2[35] proposed by Grimme was used to describe the interaction between MXenes and adatoms, because of its excellent description of long-range van der Waals interactions. The kinetic energy cut-off of 500 eV was applied for the plane-wave expansion of valence electron wave functions. The Brillouin zone was sampled using a Monkhorst-Pack k-point mesh scheme, and the meshes of Γ-centered 15×15×1 and 5×5×1 were used for the unit cell and the 3×3 supercell, respectively. To avoid the interlayer interaction, the vacuum distance of 20Å was used. The convergence criteria for energy and force were set to be 10^{-5} eV and 0.01 eV $Å^{-1}$, respectively. The charge redistribution and transfer were quantitatively studied by the charge differential analysis. Bader charge method[36] was used to estimate the amount of charge transfer between the adatoms and host material. The climbing image nudged elastic band (CI-NEB)[37] method was applied to calculate the potential energy diffusion pathway and the minimum diffusion energy barrier of metal ions on the V_3C_2 MXenes.

To investigate the dynamical stability, the Phonopy code[38] was used to calculate the phonon dispersion spectra. Additionally, *ab initio* molecular dynamics (AIMD) simulations with Nosé-

Hoover thermostat[39] and NVT ensemble were carried out to examine the thermal stability by using a 3 × 3 supercell at 300 K with the time step of 2 fs.

3. Results and discussion

3.1 Structures and stability of V_3C_2 monolayer

The V_3C_2 monolayer is built up of quintuple layers stacked in a sequence of V(2)–C–V(1)–C–V(2), which can be viewed as three V atomic layers interleaved with two C atomic layers, forming an edge-shared V_6C octahedron (Figure 1a and 1b). The optimized V_3C_2 monolayer has the lattice parameters of $a = b = 2.95$ Å and the thickness of $d = 4.43$ Å. The bond length of V(1)-C (2.11 Å) is much longer than V(2)-C (1.96 Å) due to the difference of chemical environment between V(1) and V(2).

To evaluate the structural stability of V_3C_2 monolayer, we investigate the dynamical and thermal stabilities by using the phonon dispersion spectra and AIMD simulations. In the phonon dispersion spectra calculated with GGA pseudopotential, the absence of imaginary phonon modes in the first Brillouin zone (Figure 1c) indicates that V_3C_2 monolayer is dynamically stable. Besides, after performing AIMD simulations for 10 ps, no obvious structural reconstructions can be noticed, and the total energy and temperature of the system oscillate around the equilibrium values, suggesting the thermal stability (Figure 1d).

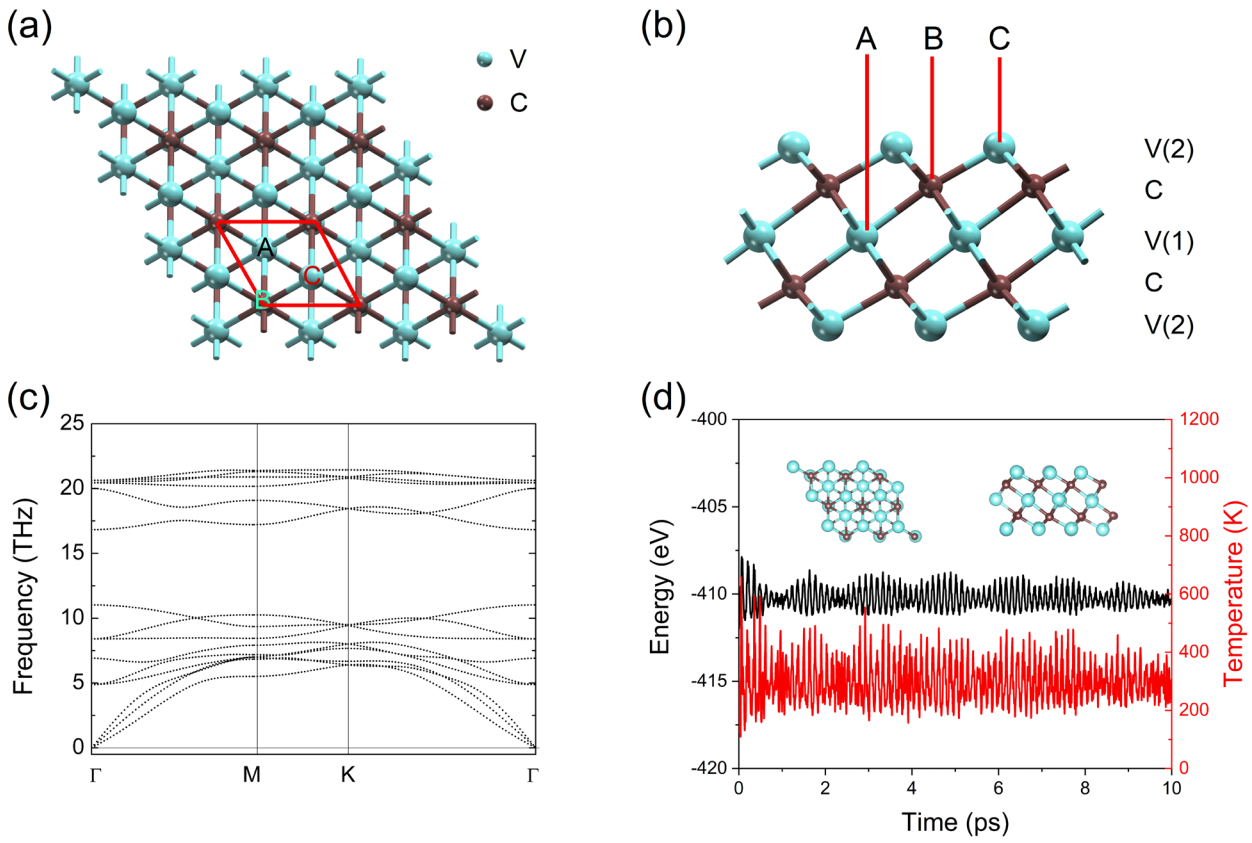

Figure 1. (a) Top and (b) side views of V_3C_2 monolayer. A, B, and C represent three possible adsorption sites for adatoms. (c) The phonon dispersion spectra of V_3C_2. (d) Total energy and temperature as a function of time for V_3C_2 during the AIMD simulation (inset: the structures of V_3C_2 after 10 ps AIMD simulation).

3.2 Single metal atom adsorption and electronic properties of V_3C_2 monolayer

To systematically study the adsorption properties, a 3×3×1 supercell is used to examine the adsorption sites for an isolated alkali metal atom (Li/Na/K/Ca). The supercell size has been tested to avoid the interaction between the adatoms deposited on different sites. Three possible high-symmetry adsorption sites A, B, and C as shown in Figure 1a and 1b are considered on the V_3C_2. The adsorption behavior and the favorable adsorption sites are quantitatively examined by comparing the adsorption energies E_{ad} calculated with the following equation:

$$E_{ad} = (E_{V_3C_2M_X} - E_{V_3C_2} - \mathrm{x}E_M)/\mathrm{x} \qquad (1)$$

here, $E_{V_3C_2M_X}$(M=Li, Na, K, or Ca) and $E_{V_3C_2}$ are the total energies of V_3C_2 with and without alkali metal atom adsorption, respectively. E_M represents the energy per metal atom in the bulk form, and x corresponds to the number of metal atoms in the adsorption configurations. Metal ion adsorption on V_3C_2 produces negative E_{ad} on all A, B, or C sites, as shown in Figure 2. For a single adatom, site A is the most favorable adsorption site as it has the smallest E_{ad} for all four systems.

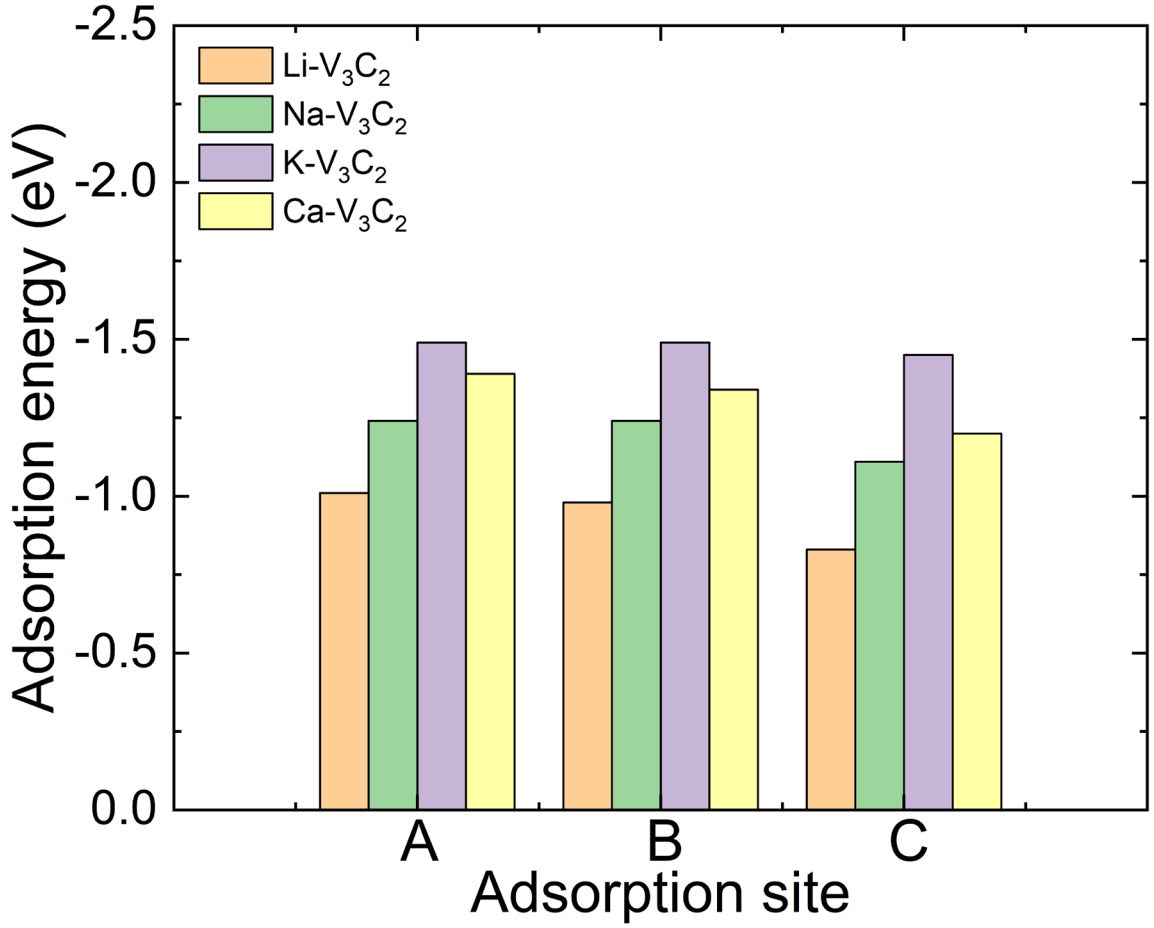

Figure 2. Adsorption energies of Li, Na, K, and Ca on V_3C_2 monolayer at A, B, and C sites.

It is suggested that the adatom height *h*, which is defined as the vertical distance between the adatom and the topmost surface atom, can also reflect the adsorption strength on different sites.[2] The adatom heights for sites A, B and C sites are listed in Table 1. For site A and B, the adatoms have similar height, while for C, the height is much larger. This is consistent with the calculated E_{ad} results, where stronger adsorption (more negative adsorption energy values) at sites A, B, and C always corresponds to a shorter adatom height *h* for all the systems (Table 1).

Table 1. Energetic and structural properties of metal atoms on V_3C_2 monolayer

	E_{ad} (eV)			Charge transfer q (e^-)			h (Å)		
	A	B	C	A	B	C	A	B	C
Li-V_3C_2	-1.01	-0.98	-0.83	0.85	0.85	0.85	2.22	2.25	2.42
Na-V_3C_2	-1.24	-1.24	-1.11	0.70	0.71	0.72	2.57	2.57	2.79
K-V_3C_2	-1.49	-1.49	-1.45	0.76	0.76	0.76	3.00	3.01	3.06
Ca-V_3C_2	-1.39	-1.34	-1.20	1.04	1.04	1.05	2.55	2.57	2.64

Electronic structure is one of the most important factors for battery performance. Here, we perform the electronic structure calculations to study the intrinsic attributes of the metal-adsorbed systems. Figure 3 shows the computed total density of states (TDOS) and projected density of states (PDOS) for these metal-adsorbed systems. It is found that the DOS at the Fermi level for all these systems are dominated by V 4*d* orbital. There is an obvious overlap at -0.69 eV below the Fermi level between Li 2*s* orbital and V 4*d* orbital, indicating *s*-*d* hybridization and strong interaction between Li adatom and V atom on the V_3C_2 surface. Similarly, for Na-V_3C_2, K-V_3C_2 and Ca-V_3C_2, the *s*−*d* hybridizations are also observed with peaks located at -0.68, -0.59, and -

0.75 eV, respectively. In addition, it is noteworthy that the systems maintain their metallic nature after the adsorption. The metallic character can ensure the good electronic conduction for both metal-adsorbed and the pristine monolayer (Figure S1), a feature that is indispensable for an ideal battery electrode.

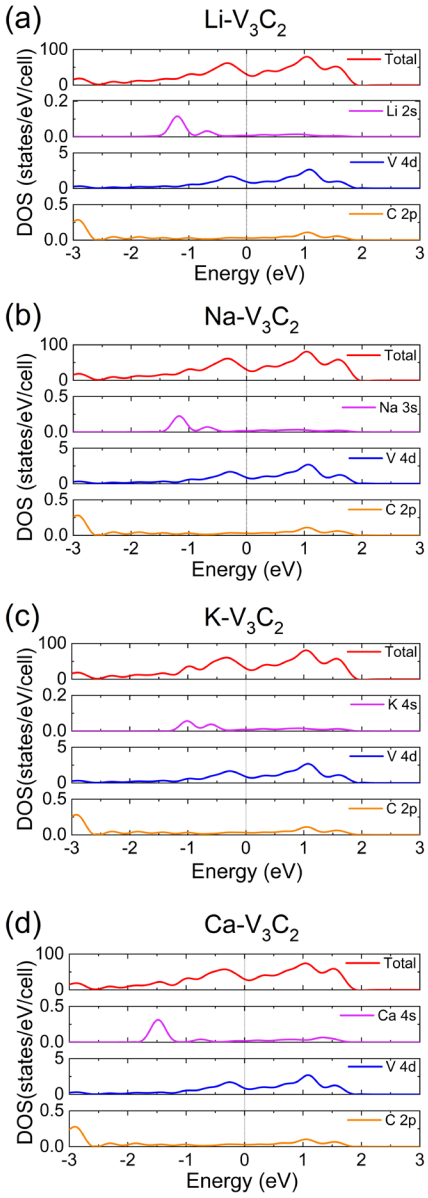

Figure 3. Total and partial density of states (DOS) for (a) Li-V_3C_2, (b) Na-V_3C_2, (c) K-V_3C_2, and (d) Ca-V_3C_2. The Fermi level is set to zero and shown in the dashed line. Partial DOS are calculated by averaging the contribution of each atom for a certain element.

To visualize the effects of adatom adsorption on the charge distribution, we calculate the differential charge density which is obtained as the difference between the valence charge density before and after the bonding (Figure 4):

$$\Delta\rho = \rho_{V_3C_2M} - \rho_M - \rho_{V_3C_2} \qquad (2)$$

where $\rho_{V_3C_2M}$ (M=Li/Na/K/Ca), ρ_M, and $\rho_{V_3C_2}$ represent the charge density distributions of M–V_3C_2 monolayer, an isolated metal atom, and bare V_3C_2. The differential charge distributions in Figure 4 clearly show the charge transfer from the adatoms to the substrates. For all four adsorption systems, the adsorbed metal atoms donate electrons to V_3C_2, mainly to the coordinated V atoms. The amount of charge transfer is estimated quantitatively by using the Bader charge analysis and the results are presented in Table 1. We find that the number of transferred electrons in Ca-V_3C_2 is the highest, which is consistent with the fact that multivalent ion Ca may transfer more than one electron per ion. Moreover, from Figure 4 we can see that a built-in electric field is introduced to the system with metal atom adsorption due to the spatial separation of electron and hole, which leads to extended electron-hole recombination time.[40]

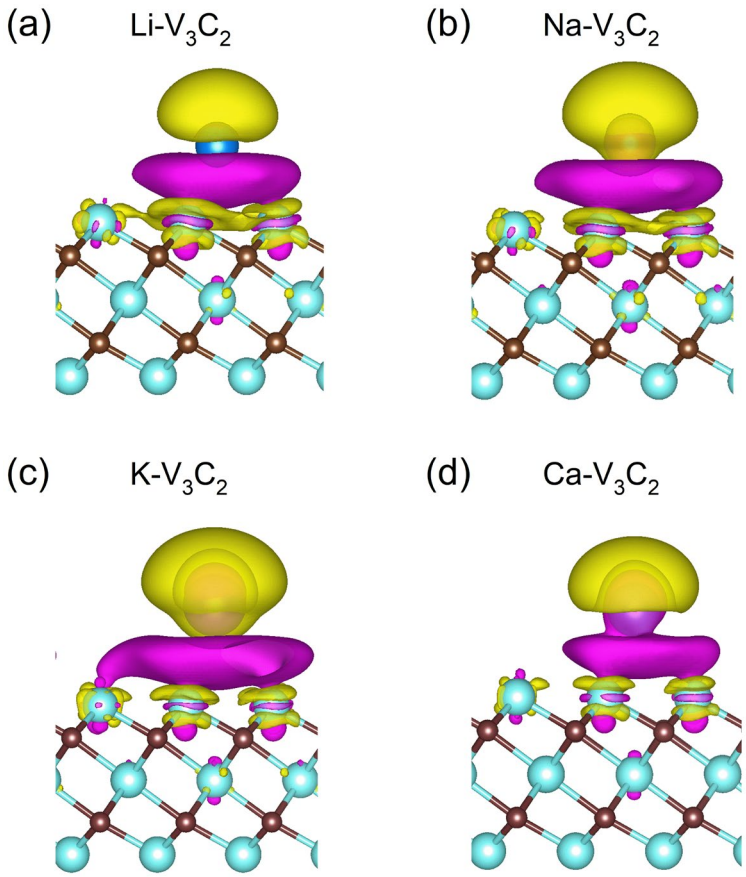

Figure 4. Differential charge density distributions of (a) Li-V_3C_2, (b) Na-V_3C_2, (c) K-V_3C_2, and (d) Ca-V_3C_2. Pink and yellow colours indicate electron accumulation and depletion, respectively.

3.3 Metal ion diffusion on V_3C_2 monolayer

The charge-discharge rate, which depends on the mobility of the intercalating ions, is another significant character for assessing the capability of an electrode material for rechargeable batteries. Therefore, we turn to the motion of metal ions on the MXene and investigate the diffusion barriers for metal ions on the V_3C_2 monolayer using the CI-NEB method. We consider three possible diffusion paths denoted as Path 1, Path 2 and Path 3 by black, red, and blue arrows (Figure 5a), which connect the two neighboring most preferable adsorption sites. For all four systems (Figure

5b-5e), the calculated lowest diffusion barriers are along Path 2 and the values are 0.04, 0.02, 0.01, and 0.04 eV for Li, Na, K, and Ca, respectively. Similar to reference[23], the fact that Path 2 has the lowest diffusion barrier is consistent with our adsorption energy calculation results, since Path 2 goes through site B, which has lower adsorption energy values for Li, Na, K, and Ca on V_3C_2 monolayer (Table 1). On the other hand, Paths 1 and 3 pass through or near site C with adsorption energy values much larger than those on site B. We note that the diffusion barriers on V_3C_2 are far smaller than that on typical 2D materials such as graphene (0.33 eV)[9, 41], MoS_2 (0.25 eV)[20, 42], MoN_2 (0.78 eV)[3], and phosphorene (0.13–0.76 eV)[43-44]. This can be attributed to the fact that metal ions have close E_{ad} values on different high-symmetry adsorption sites of V_3C_2 (Table 1). The low barriers ensure that alkali metal ions can migrate easily on the surface of our studied systems. Therefore, 2D V_3C_2 can be promising electrode materials with fast charge-discharge rate and good rate capability.

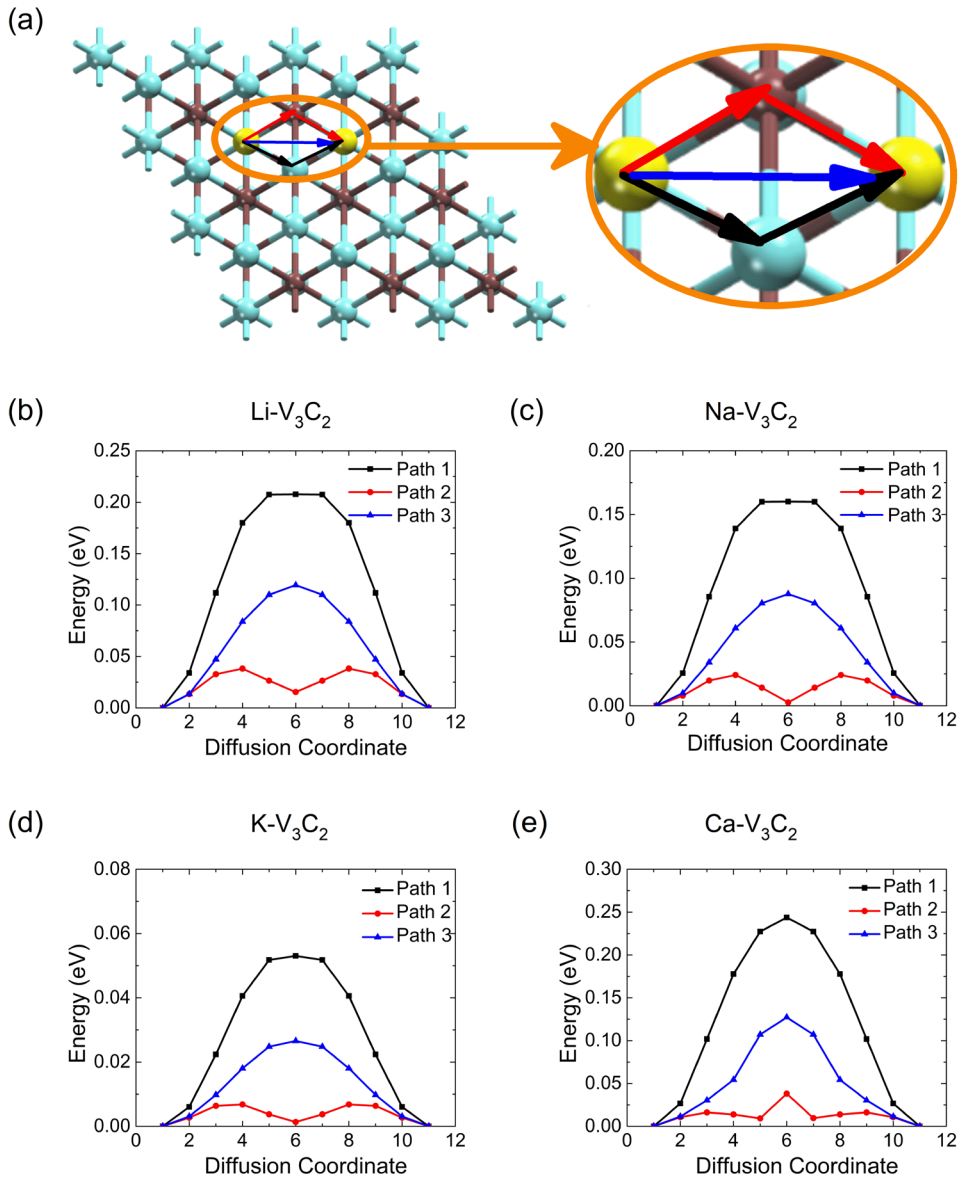

Figure 5. (a) Schematic representation of three possible migration paths of Li and Na diffusion on the V_3C_2 monolayer, and the corresponding diffusion barrier profiles of (b) Li-V_3C_2, (c) Na-V_3C_2, (d) K-V_3C_2, and (e) Ca-V_3C_2.

3.4 Theoretical open circuit voltage and storage capacity

For practical applications, the storage capacity of the batteries is the key indicator for the performance of the electrode materials and the current focus for improvement. To explore the maximum storage capacity for metal atoms, we consider the adsorption with an increasing number of adsorbed metal atoms on both sides of the V_3C_2 monolayer in the 3×3 supercell. To obtain more accurate results, the ground state structure should be determined as the structure with the lowest energy, after taking all possible adsorption structures into consideration (Figure S2 and Table S1). Both the atomic positions and lattice constants are fully relaxed for the configurations after the intercalation. As mentioned above, we assign the first metal adsorption layer at the A site. The charge/discharge processes can be described by the following half-cell reactions:

$$V_3C_2 + xM^+ + xe^- \leftrightarrow V_3C_2M_X \qquad (3)$$

The open circuit voltage (OCV) at different coverage on the surfaces of the V_3C_2 is calculated as: [3, 18, 45]

$$OCV \approx (E_{V_3C_2} + \mathrm{x}E_M - E_{V_3C_2M_X})/\mathrm{x} \qquad (4)$$

The calculated OCV as a function of the number of adatoms on the V_3C_2 supercell is plotted in Figure 6a. We can see that the curves for all metal show similar trend that OCV decreases as x increases. It is noteworthy that OCV for both K and Ca shows negative values when x reaches 2, indicating that K (Ca) cannot realize the complete coverage of the surface of V_3C_2 monolayer. On the other hand, the OCV for Li/Na shows multilayer adsorption features, since the values are still positive when x reaches 4.

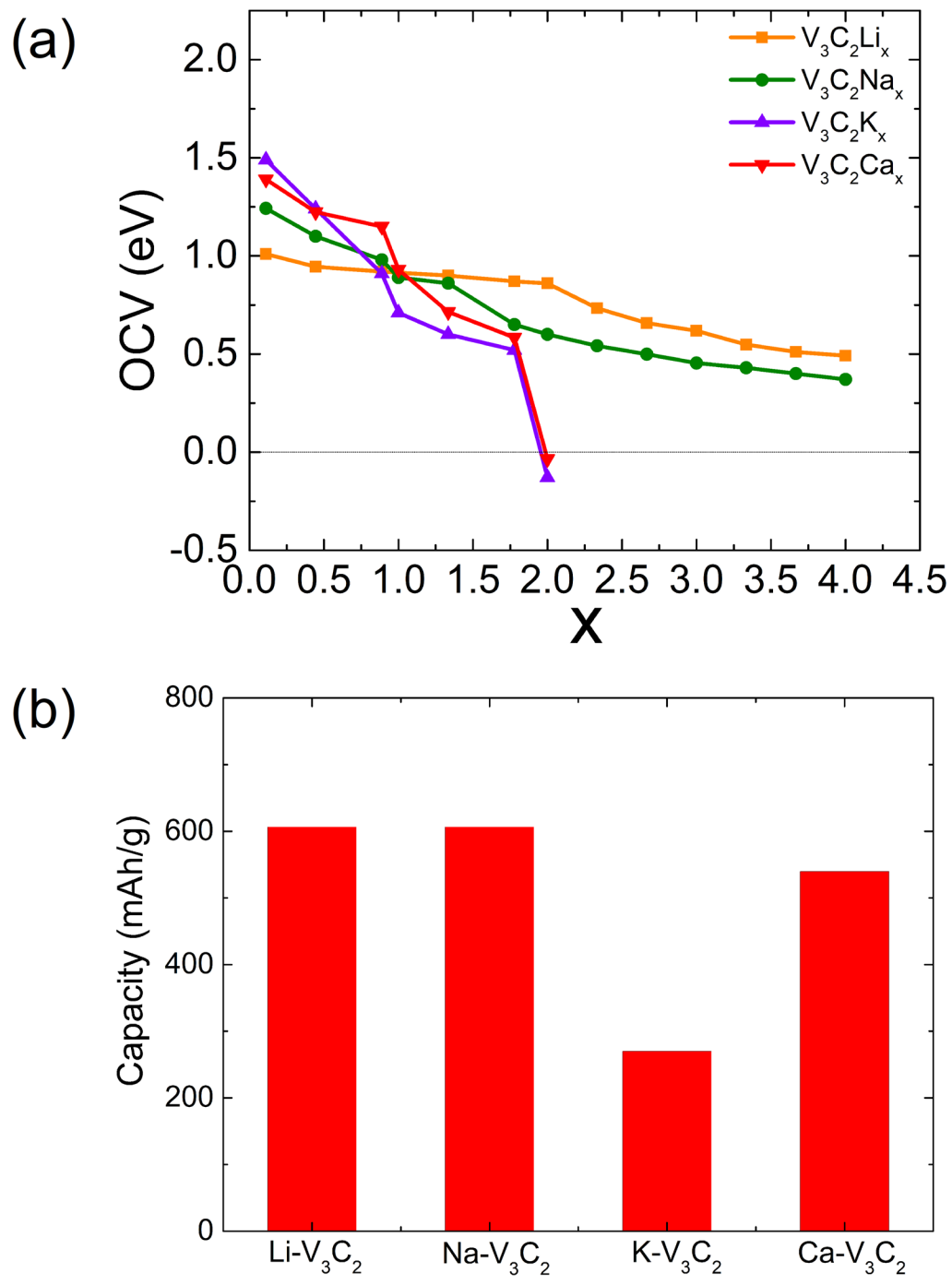

Figure 6. (a) OCV as a function of x and (b) maximum capacity for $V_3C_2Li_x$, $V_3C_2Na_x$, $V_3C_2K_x$, and $V_3C_2Ca_x$.

To further analyze the multilayer adsorption patterns for Li/Na on V_3C_2, the layer-resolved average adsorption energies are obtained by calculating the total energy differences before and after the intercalation of a new Li/Na layer. The average adsorption energy (E_{ave}) is defined as:

$$E_{ave} = (E_{V_{27}C_{18}M_{18n}} - E_{V_{27}C_{18}M_{18(n-1)}} - 18E_M)/18 \qquad (5)$$

where $E_{V_{27}C_{18}M_{18n}}$ and $E_{V_{27}C_{18}M_{18(n-1)}}$ are the total energies of V_3C_2 with n and (n−1) adsorption layers, respectively, and the number 18 corresponds to 18 adatoms for each layer. For the first adsorption layer of V_3C_2, the calculated average adsorption energies are -0.87 eV and -0.60 eV per atom for Li and Na (Table 2). The large negative adsorption energy values ensure good adsorption stabilities. For the second adsorption layer, on the other hand, the E_{ave} for Li/Na on V_3C_2 (on site B) are close to zero, indicating weak multilayer adsorption. Considering the average adsorption energy, V_3C_2 can accommodate up to two layers of Li/Na ions (Figure 7). These values are comparable to some typical electrode materials, such as Na on $Ti_3C_2O_2$ (-0.01 eV per atom)[11], and GeS (−0.02 eV per atom).[3] It is feasible to use these values to estimate the theoretical maximum capacity.

Table 2. The comparison of Li/Na adsorption and diffusion parameters on the V_3C_2 and $V_3C_2O_2$ monolayer.

Energy	$E_1^a(eV)$	$E_{diff}^b(eV)$	$E_{1st}^c(eV)$	$E_{2nd}^d(eV)$
V_3C_2-Li	-1.01	0.04	-0.87	-0.12
V_3C_2-Na	-1.24	0.02	-0.60	-0.14
$V_3C_2O_2$-Li	-2.92	0.30	-1.74	-0.01
$V_3C_2O_2$-Na	-2.73	0.31	-1.06	-0.05

E_1^a--the adsorption energy of one Li/Na atom; E_{diff}^b--the diffusion barrier of one Li/Na atom; E_{1st}^c--the average adsorption energy of the first-layer Li/Na atoms; E_{2nd}^d--the average adsorption energy of the second-layer Li/Na atoms.

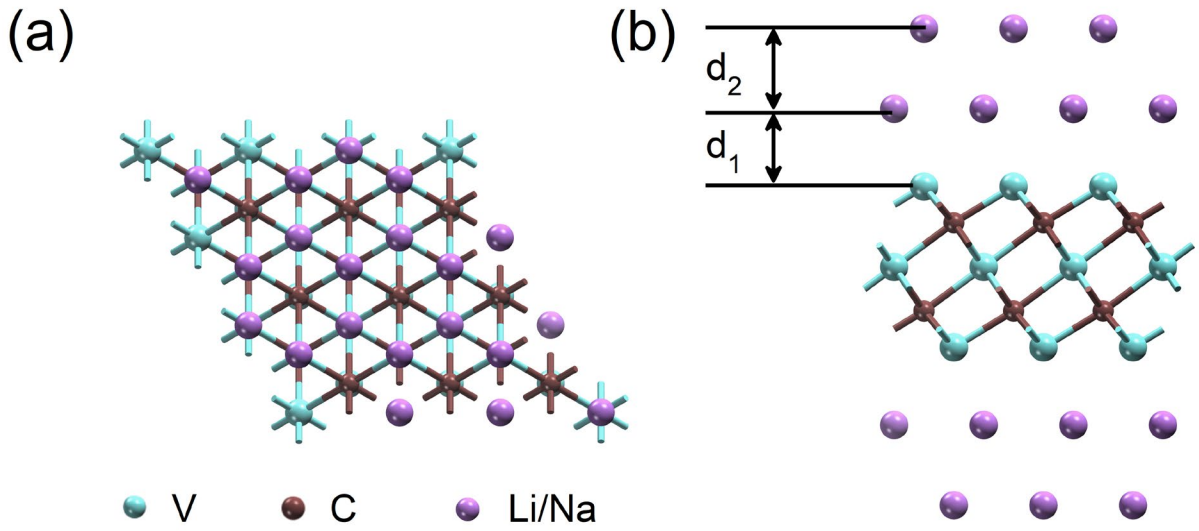

Figure 7. Geometric structures for Li/Na adsorption on the V_3C_2 monolayer from (a) top and (b) side views.

In addition, the distances between the adatoms and the substrates play an important role in investigating the adsorption ability of anode materials. We find that the distance between the first

layer of Li (Na) and the host V_3C_2 monolayer (d_1) is 2.19 (2.58) Å, and that between the second layer and the first layer (d_2) is 2.26 (2.98) Å. Due to the large distance between the second Li/Na layer and the substrates, the corresponding chemical interactions are so weak that it is reasonable not to consider the third metal layer.

Meanwhile, the maximum capacity (C_M) can be obtained by the following equation:[3, 46]

$$C_M \approx zx_{max}\mathrm{F}/M_{V_3C_2} \qquad (6)$$

where z is the valence number, x_{max} represents the maximum adatom content, F is the Faraday constant (26.8 Ahmol^{-1}) and $M_{V_3C_2}$ is the relative molecular mass of V_3C_2. The maximum capacities for V_3C_2 are calculated to be 606.42 mAh g^{-1} (x_{max} =4) of both Li and Na, 269.86 mAh g^{-1} (x_{max} =1.78) for K and 539.71 mAh g^{-1} (x_{max} =1.78) for Ca (Figure 6b), highlighting V_3C_2 MXenes as promising high-capacity anode materials for metal ion batteries, especially for LIBs/SIBs.

Since the carrier density in the V_3C_2 is largely provided by the V 4*d* and adatom's *s* orbitals near the Fermi level, the interaction between the Li (Na) and the MXene can be further revealed from its localized electrons. Therefore, we calculate the electron localization functions (ELF) of the (110) section (Figure S3) of the V_3C_2 monolayer with one and two layers of Li or Na (Figure 8) to obtain the insights into the physical origin of the predicted multilayer adsorption patterns. The electrons over the first Na layer are spread like the free electron gas, forming a negatively charged cloud, while there is no negatively charged cloud over the Li layer (Figure 8a and 8c). For the second layer, we find plentiful electrons concentrated between the first and second layer of Li atoms, implying a strong bonding between them (Figure 8b). However, for Na system, we can

observe the negatively charged cloud over the Na layer, which means the second Na layer can bind with the V_3C_2 monolayer stronger, and the extra layer of Na atoms is less likely to form clusters than Li (Figure 8d). The ELF plots explain the multilayer adsorption behavior of Li/Na on the V_3C_2 monolayer.

The lattice mismatch is another significant factor for the recycling and stability of batteries which needs to be considered. Thus, we optimize the lattice constants of V_3C_2 monolayer without and with atoms adsorption. The largest variation of the lattice constants for all four systems is only 0.6 % (Table S2), indicating that V_3C_2 monolayer does not suffer a lot from structural changes during charge/discharge, which is ideal for practical applications.

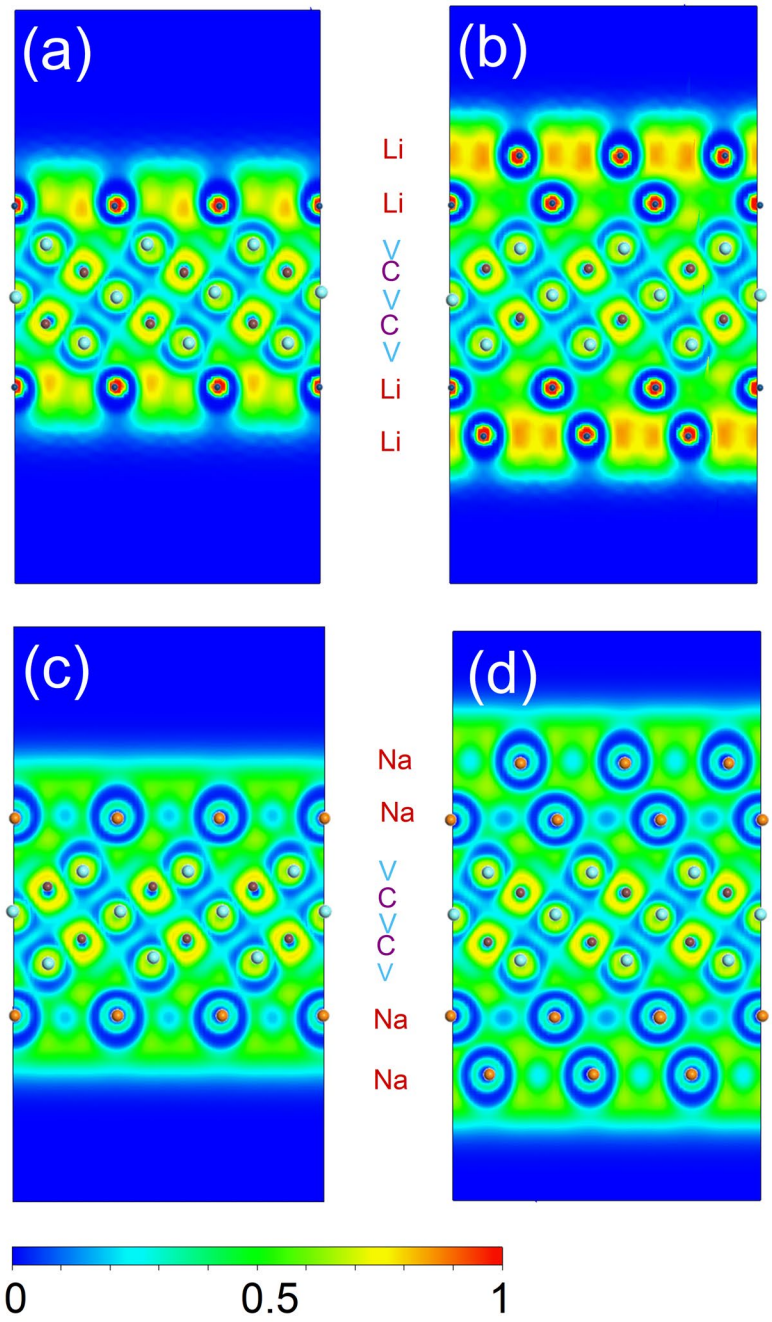

Figure 8. The electron localization functions (ELF) of the (110) section of the V_3C_2 monolayer for (a) Li-V_3C_2, (b) Li_2-V_3C_2, (c) Na-V_3C_2, and (d) Na_2-V_3C_2. The scale bar shows the isodensity values of ELF.

3.5 Investigation of O-functionalized V_3C_2 as anode materials for LIBs/SIBs

During the experimental synthesis of MXenes with the formula of $M_{n+1}AX_n$ (n = 1, 2, or 3), A atoms can be replaced by terminal groups such as -O.[47-51] Experimental and theoretical studies have shown that the energy storage capacities of MXenes may depend on the nature of surface terminal groups, therefore, the properties associated with those groups are worthy of further exploring. [9-10, 14, 28, 31, 52] In this part, we further study $V_3C_2O_2$ monolayer as anode material for LIBs/SIBs, since O-terminated Ti_2C, V_2C, Cr_2C, and Ti_3C_2, and Zr_3C_2 are reported to be good candidates.[10, 53-54]

$V_3C_2O_2$ MXene is constructed by adsorbing O atoms on the most stable site of the V_3C_2 monolayer (Figure S4). Compared with V_3C_2, the optimized O-terminated monolayer has smaller in-plane lattice parameters $a = b = 2.91$ Å and larger thickness $d = 5.82$ Å. With the terminal O atoms, the bond length of V(1)–C shrinks, while that of V(2)-C is elongated (Table S3), implying that the terminal atoms strongly interact with the original V_3C_2 monolayer. Besides, the Li/Na atom absorption on $V_3C_2O_2$ monolayer shows smaller adsorption value than that on V_3C_2, implying that Li/Na-$V_3C_2O_2$ are more stable structures (Table 2).

For Li and Na adsorbed on the $V_3C_2O_2$ monolayer, the diffusion barriers are much larger than V_3C_2 (Table 2 and Figure S5), but still comparable to or smaller than other 2D materials. This phenomenon can be ascribed to the surface O adsorption since the bonding strength between the adatom and non-metallic surface atoms is much stronger than that with metallic surface atoms.

The OCVs for Li/Na on the surface of $V_3C_2O_2$ monolayer are higher than the bare V_3C_2 monolayer, and the maximum capacities for $V_3C_2O_2$ are calculated to be 513.5 mAh g^{-1} of both Li and Na (Figure S6). ELF results show that for the Li/Na ion adsorption in $V_3C_2O_2$, the bonds

between O and adatom (Li or Na) show ionic bond character, and both the electrons over the Li layer and Na layer form a negatively charged cloud (Figure S7). Comparing with the configurations given in Figure 8, more electrons may transfer from the inner layer to the outer layer of Li atoms for $V_3C_2O_2$ than V_3C_2, which is consistent with OCV results. To sum up, $V_3C_2O_2$ monolayer, despite its slightly higher barriers and smaller capacity values than V_3C_2, still shows good properties among 2D energy materials due to the strong adsorption energy and high OCV.

4. Conclusions

In summary, we have explored the potential applications of V_3C_2 MXene as the anode materials for alkali metal (Li/Na/K/Ca) batteries by means of DFT computations. We have identified the most energetically favorable diffusion pathways for metal atoms in this material with considerably low diffusion barriers of 0.04 eV for Li, 0.02 eV for Na, 0.01 eV for K, and 0.04 eV for Ca, thus possess good charge-discharge rates as electrodes. In addition, the average adsorption energy, as well as ELF results reveal the origin of the multilayer adsorption behavior of V_3C_2, with high theoretical capacity values of 606.42 mAh g^{-1} for both Li and Na. Our results give insightful prospects for further experimental work to explore the V_3C_2 monolayer as promising electrode material for metal ion batteries, especially for the LIBs and the newly-developed SIBs.

ASSOCIATED CONTENT

Supporting Information.

The following files are available free of charge.

Lattice parameters; density of states for V_3C_2 and $V_3C_2O_2$; structure of adsorption sites for adatoms; schematic representation of the crystallographic orientation along (110) section; migration paths and diffusion barrier profiles of Li-$V_3C_2O_2$ and Na-$V_3C_2O_2$; OCV as a function of x and maximum capacity for Li/Na-V_3C_2/$V_3C_2O_2$; ELF for Li/Li_2/Na/Na_2-$V_3C_2O_2$.

AUTHOR INFORMATION

Notes

The authors declare no competing financial interests.

ACKNOWLEDGMENT

This work was supported by the Research Grants Council of the Hong Kong Special Administrative Region, China (Project No. PolyU152208/18E), the Hong Kong Polytechnic University (Project Nos. RHA3 and G-UABC), and NSFC (No. 11804286).

REFERENCES

1. Chen, H.; Cong, T. N.; Yang, W.; Tan, C.; Li, Y.; Ding, Y., Progress in electrical energy storage system: A critical review. *Prog. Nat. Sci.* **2009**, *19*, 291-312.

2. Er, D.; Li, J.; Naguib, M.; Gogotsi, Y.; Shenoy, V. B., Ti_3C_2 MXene as a high capacity electrode material for metal (Li, Na, K, Ca) ion batteries. *ACS Appl. Mater. Interfaces* **2014**, *6*, 11173-11179.

3. Zhang, X.; Yu, Z.; Wang, S.-S.; Guan, S.; Yang, H. Y.; Yao, Y.; Yang, S. A., Theoretical prediction of MoN_2 monolayer as a high capacity electrode material for metal ion batteries. *J. Mater. Chem. A* **2016**, *4*, 15224-15231.

4. Sun, Q.; Dai, Y.; Ma, Y.; Jing, T.; Wei, W.; Huang, B., Ab Initio Prediction and Characterization of Mo_2C Monolayer as Anodes for Lithium-Ion and Sodium-Ion Batteries. *J. Phys. Chem. Lett.* **2016**, *7*, 937-43.

5. Pan, H.; Hu, Y.-S.; Chen, L., Room-temperature stationary sodium-ion batteries for large-scale electric energy storage. *Energy Environ. Sci.* **2013**, *6*, 2338-2360.

6. Lan, Z.; Chen, M.; Xu, X.; Xiao, C.; Wang, F.; Wang, Y.; Lu, Y.; Jiang, Y.; Jiang, J., Investigations on molybdenum dinitride as a promising anode material for Na-ion batteries from first-principle calculations. *J. Alloys Compd.* **2017**, *701*, 875-881.

7. Jiang, H. R.; Shyy, W.; Liu, M.; Wei, L.; Wu, M. C.; Zhao, T. S., Boron phosphide monolayer as a potential anode material for alkali metal-based batteries. *J. Mater. Chem. A* **2017**, *5*, 672-679.

8. Lv, X.; Wei, W.; Huang, B.; Dai, Y., Achieving high energy density for lithium-ion battery anodes by Si/C nanostructure design. *J. Mater. Chem. A* **2019**, *7*, 2165-2171.

9. Meng, Q.; Hu, A.; Zhi, C.; Fan, J., Theoretical prediction of MXene-like structured Ti_3C_4 as a high capacity electrode material for Na ion batteries. *Phys. Chem. Chem. Phys.* **2017**, *19*, 29106-29113.

10. Meng, Q.; Ma, J.; Zhang, Y.; Li, Z.; Hu, A.; Kai, J.-J.; Fan, J., Theoretical investigation of zirconium carbide MXenes as prospective high capacity anode materials for Na-ion batteries. *J. Mater. Chem. A* **2018**, *6*, 13652-13660.

11. Meng, Q.; Ma, J.; Zhang, Y.; Li, Z.; Zhi, C.; Hu, A.; Fan, J., The S-functionalized Ti_3C_2 MXene as a high capacity electrode material for Na-ion batteries: a DFT study. *Nanoscale* **2018**, *10*, 3385-3392.

12. Zhang, D.; Ding, Z.; Yang, Y.; Zhao, S.; Huang, Q.; Chen, C.; Chen, L.; Wei, W., Fabricating 3D ordered marcoporous Na_2MnSiO_4/C with hierarchical pores for fast sodium storage. *Electrochim. Acta* **2018**, *269*, 694-699.

13. Eftekhari, A., Potassium secondary cell based on Prussian blue cathode. *J. Power Sources* **2004**, *126*, 221-228.

14. Tang, Q.; Zhou, Z.; Shen, P., Are MXenes promising anode materials for Li ion batteries? Computational studies on electronic properties and Li storage capability of Ti_3C_2 and $Ti_3C_2X_2$ (X = F, OH) monolayer. *J. Am. Chem. Soc.* **2012**, *134*, 16909-16.

15. Jung, S. C.; Choi, J.-H.; Han, Y.-K., The origin of excellent rate and cycle performance of Sn_4P_3 binary electrodes for sodium-ion batteries. *J. Mater. Chem. A* **2018**, *6*, 1772-1779.

16. Wang, S.; Yang, B.; Chen, H.; Ruckenstein, E., Popgraphene: a new 2D planar carbon allotrope composed of 5–8–5 carbon rings for high-performance lithium-ion battery anodes from bottom-up programming. *J. Mater. Chem. A* **2018**, *6*, 6815-6821.

17. Pan, H., Electronic properties and lithium storage capacities of two-dimensional transition-metal nitride monolayers. *J. Mater. Chem. A* **2015**, *3*, 21486-21493.

18. Yang, E.; Ji, H.; Jung, Y., Two-Dimensional Transition Metal Dichalcogenide Monolayers as Promising Sodium Ion Battery Anodes. *J. Phys. Chem. C* **2015**, *119*, 26374-26380.

19. Li, P.; Li, Z.; Yang, J., Rational Design of Two-dimensional Anode Materials: B_2S as a Strained Graphene. *J. Phys. Chem. Lett.* **2018**, *9*, 4852-4856.

20. Liu, C.-S.; Yang, X.-L.; Liu, J.; Ye, X.-J., Theoretical Prediction of Two-Dimensional SnP_3 as a Promising Anode Material for Na-Ion Batteries. *ACS Appl. Energy Mater.* **2018**, *1*, 3850-3859.

21. Shukla, V.; Araujo, R. B.; Jena, N. K.; Ahuja, R., Borophene's tryst with stability: exploring 2D hydrogen boride as an electrode for rechargeable batteries. *Phys. Chem. Chem. Phys.* **2018**, *20*, 22008-22016.

22. Shukla, V.; Jena, N. K.; Naqvi, S. R.; Luo, W.; Ahuja, R., Modelling high-performing batteries with MXenes: The case of S-functionalized two-dimensional nitride MXene electrode. *Nano Energy* **2019**, *58*, 877-885.

23. Zhang, T.; Ma, Y.; Huang, B.; Dai, Y., Two-Dimensional Penta-BN_2 with High Specific Capacity for Li-Ion Batteries. *ACS Appl. Mater. Interfaces* **2019**, *11*, 6104-6110.

24. Lopez, H. A.; Anguchamy, Y. K.; Deng, H.; Han, Y.; Masarapu, C.; Venkatachalam, S.; Kumar, S., High capacity anode materials for lithium ion batteries. Google Patents: 2015.

25. Seh, Z. W.; Fredrickson, K. D.; Anasori, B.; Kibsgaard, J.; Strickler, A. L.; Lukatskaya, M. R.; Gogotsi, Y.; Jaramillo, T. F.; Vojvodic, A., Two-Dimensional Molybdenum Carbide (MXene) as an Efficient Electrocatalyst for Hydrogen Evolution. *ACS Energy Letters* **2016**, *1*, 589-594.

26. Anasori, B.; Lukatskaya, M. R.; Gogotsi, Y., 2D metal carbides and nitrides (MXenes) for energy storage. *Nat. Rev. Mater.* **2017**, *2*, 16098.

27. Naguib, M.; Unocic, R. R.; Armstrong, B. L.; Nanda, J., Large-scale delamination of multi-layers transition metal carbides and carbonitrides "MXenes". *Dalton Trans.* **2015**, *44*, 9353-9358.

28. Chen, X.; Kong, Z.; Li, N.; Zhao, X.; Sun, C., Proposing the prospects of Ti_3CN transition metal carbides (MXenes) as anodes of Li-ion batteries: a DFT study. *Phys. Chem. Chem. Phys.* **2016**, *18*, 32937-32943.

29. Yu, T.; Zhang, S.; Li, F.; Zhao, Z.; Liu, L.; Xu, H.; Yang, G., Stable and metallic two-dimensional TaC_2 as an anode material for lithium-ion battery. *J. Mater. Chem. A* **2017**, *5*, 18698-18706.

30. Anasori, B.; Xie, Y.; Beidaghi, M.; Lu, J.; Hosler, B. C.; Hultman, L.; Kent, P. R.; Gogotsi, Y.; Barsoum, M. W., Two-dimensional, ordered, double transition metals carbides (MXenes). *ACS Nano* **2015**, *9*, 9507-9516.

31. Hu, J.; Xu, B.; Ouyang, C.; Yang, S. A.; Yao, Y., Investigations on V_2C and V_2CX_2 (X = F, OH) Monolayer as a Promising Anode Material for Li Ion Batteries from First-Principles Calculations. *J. Phys. Chem. C* **2014**, *118*, 24274-24281.

32. Azofra, L. M.; Li, N.; MacFarlane, D. R.; Sun, C., Promising prospects for 2D d^2–d^4 M_3C_2 transition metal carbides (MXenes) in N_2 capture and conversion into ammonia. *Energy Environ. Sci.* **2016**, *9*, 2545-2549.

33. Kresse, G.; Furthmüller, J., Efficient iterative schemes for ab initio total-energy calculations using a plane-wave basis set. *Phys. Rev. B* **1996**, *54*, 11169.

34. Perdew, J. P.; Burke, K.; Ernzerhof, M., Generalized gradient approximation made simple. *Phys. Rev. Lett.* **1996**, *77*, 3865.

35. Grimme, S., Semiempirical GGA‐type density functional constructed with a long‐range dispersion correction. *J. Comput. Chem.* **2006**, *27*, 1787-1799.

36. Tang, W.; Sanville, E.; Henkelman, G., A grid-based Bader analysis algorithm without lattice bias. *J. Phys.: Condens. Matter* **2009**, *21*, 084204.

37. Henkelman, G.; Uberuaga, B. P.; Jónsson, H., A climbing image nudged elastic band method for finding saddle points and minimum energy paths. *J. Chem. Phys.* **2000**, *113*, 9901-9904.

38. Togo, A.; Tanaka, I., First principles phonon calculations in materials science. *Scr. Mater.* **2015**, *108*, 1-5.

39. Nosé, S., A unified formulation of the constant temperature molecular dynamics methods. *J. Chem. Phys.* **1984**, *81*, 511-519.

40. Long, C.; Dai, Y.; Gong, Z.-R.; Jin, H., Robust type-II band alignment in Janus-MoSSe bilayer with extremely long carrier lifetime induced by the intrinsic electric field. *Phys. Rev. B* **2019**, *99*, 115316.

41. Lee, E.; Persson, K. A., Li absorption and intercalation in single layer graphene and few layer graphene by first principles. *Nano Lett.* **2012**, *12*, 4624-8.

42. Yu, T.; Zhao, Z.; Liu, L.; Zhang, S.; Xu, H.; Yang, G., TiC_3 Monolayer with High Specific Capacity for Sodium-Ion Batteries. *J. Am. Chem. Soc.* **2018**, *140*, 5962-5968.

43. Guo, G.-C.; Wei, X.-L.; Wang, D.; Luo, Y.; Liu, L.-M., Pristine and defect-containing phosphorene as promising anode materials for rechargeable Li batteries. *J. Mater. Chem. A* **2015**, *3*, 11246-11252.

44. Zhao, S.; Kang, W.; Xue, J., The potential application of phosphorene as an anode material in Li-ion batteries. *J. Mater. Chem. A* **2014**, *2*, 19046-19052.

45. Li, X.; Wang, Q.; Jena, P., psi-Graphene: A New Metallic Allotrope of Planar Carbon with Potential Applications as Anode Materials for Lithium-Ion Batteries. *J. Phys. Chem. Lett.* **2017**, *8*, 3234-3241.

46. Zhang, X.; Hu, J.; Cheng, Y.; Yang, H. Y.; Yao, Y.; Yang, S. A., Borophene as an extremely high capacity electrode material for Li-ion and Na-ion batteries. *Nanoscale* **2016**, *8*, 15340-7.

47. Halim, J.; Kota, S.; Lukatskaya, M. R.; Naguib, M.; Zhao, M.-Q.; Moon, E. J.; Pitock, J.; Nanda, J.; May, S. J.; Gogotsi, Y., et al., Synthesis and Characterization of 2D Molybdenum Carbide (MXene). *Adv. Funct. Mater.* **2016**, *26*, 3118-3127.

48. Lee, A.; Krishnamurthy, D.; Viswanathan, V., Exploring MXenes as Cathodes for Non-Aqueous Lithium-Oxygen Batteries: Design Rules for Selectively Nucleating Li_2O_2. *ChemSusChem* **2018**, *11*, 1911-1918.

49. Lei, J.-C.; Zhang, X.; Zhou, Z., Recent advances in MXene: Preparation, properties, and applications. *Front. Phys.* **2015**, *10*, 276-286.

50. Mashtalir, O.; Lukatskaya, M. R.; Zhao, M. Q.; Barsoum, M. W.; Gogotsi, Y., Amine-Assisted Delamination of Nb_2C MXene for Li-Ion Energy Storage Devices. *Adv. Mater.* **2015**, *27*, 3501-6.

51. Zhu, J.; Chroneos, A.; Schwingenschlögl, U., Nb-based MXenes for Li-ion battery applications. *Phys. Status Solidi-R.* **2015**, *9*, 726-729.

52. Xie, Y.; Dall'Agnese, Y.; Naguib, M.; Gogotsi, Y.; Barsoum, M. W.; Zhuang, H. L.; Kent, P. R., Prediction and characterization of MXene nanosheet anodes for non-lithium-ion batteries. *ACS Nano* **2014**, *8*, 9606-9615.

53. Yu, Y.-X., Prediction of mobility, enhanced storage capacity, and volume change during sodiation on interlayer-expanded functionalized Ti_3C_2 MXene anode materials for sodium-ion batteries. *J. Phys. Chem. C* **2016**, *120*, 5288-5296.

54. Xie, Y.; Naguib, M.; Mochalin, V. N.; Barsoum, M. W.; Gogotsi, Y.; Yu, X.; Nam, K.-W.; Yang, X.-Q.; Kolesnikov, A. I.; Kent, P. R., Role of surface structure on Li-ion energy storage capacity of two-dimensional transition-metal carbides. *J. Am. Chem. Soc.* **2014**, *136*, 6385-6394.

TOC Graphic

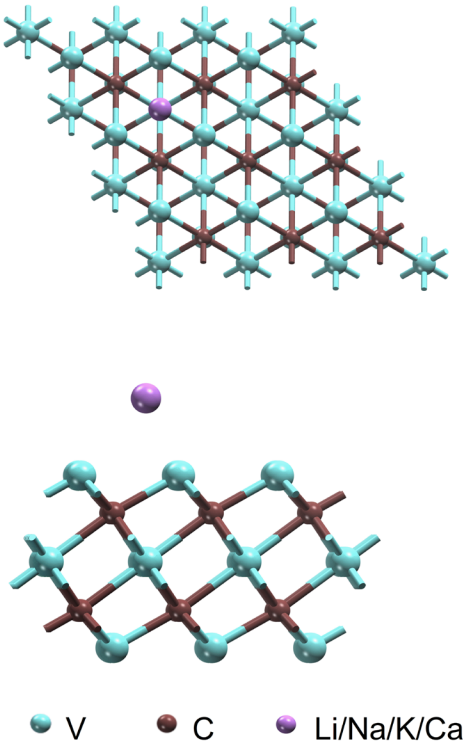
V
C
Li/Na/K/Ca

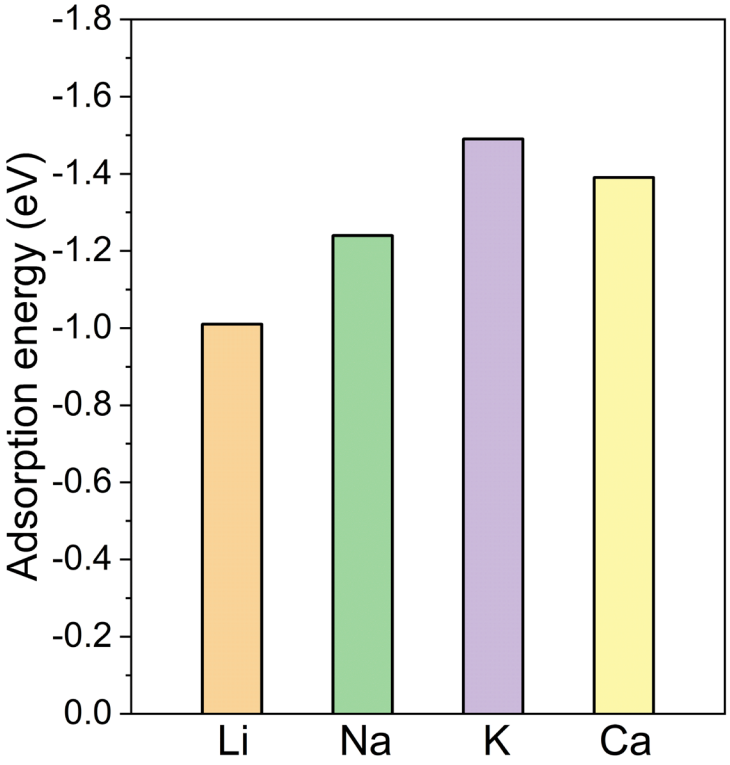
Adsorption energy (eV)
-1.8
-1.6
-1.4
-1.2
-1.0
-0.8
-0.6
-0.4
-0.2
0.0
Li
Na
K
Ca